Systematic bandgap engineering of graphene quantum dots and applications for photocatalytic water splitting and Co2 reduction

Yan, Yibo; Chen, Jie; Li, Nan; Tian, Jingqi; Li, Kaixin; Jiang, Jizhou; Liu, Jiyang; Tian, Qinghua; Chen, Peng

2018

Yan, Y., Chen, J., Li, N., Tian, J., Li, K., Jiang, J., . . . Chen, P. (2018). Systematic bandgap engineering of graphene quantum dots and applications for photocatalytic water splitting and Co2 reduction. ACS Nano, 12(4), 3523-3532. doi:10.1021/acsnano.8b00498

https://hdl.handle.net/10356/103257

https://doi.org/10.1021/acsnano.8b00498

Systematic Bandgap Engineering of Graphene Quantum Dots and Applications for Photocatalytic Water Splitting and CO_2 Reduction

*Yibo Yan[a], Jie Chen[a], Nan Li[a], Jingqi Tian[a], Kaixin Li[a], Jizhou Jiang[a], Jiyang Liu[b], Qinghua Tian[b], Peng Chen[a,]**

[a]School of Chemical and Biomedical Engineering, Nanyang Technological University, 70 Nanyang Drive, 637457, Singapore.

[b]Department of Chemistry, School of Sciences, Zhejiang Sci-Tech University, 928 Second Avenue, Xiasha Higher Education Zone, Hangzhou, China

E-mail: ChenPeng@ntu.edu.sg

ABSTRACT

Graphene quantum dot (GQD), which is the latest addition to the nanocarbon material family, promises a wide spectrum of applications. Herein, we demonstrate two different functionalization strategies to systematically tailor the bandgap structures of GQDs whereby making them snugly suitable for particular applications. Furthermore, the functionalized GQDs with a narrow bandgap and intramolecular Z-scheme structure are employed as the efficient photocatalysts for water splitting and carbon dioxide reduction under visible light. The underlying mechanisms of our observations are studied and discussed.

KEYWORDS: graphene quantum dots, bandgap engineering, photocatalysis, photoluminescence, water splitting, CO_2 reduction

2D graphene is a zero bandgap semimetal because its valence and conduction bands (π and π* orbitals) meet at the Dirac point. When the lateral dimensions of graphene sheets shrink to nanoscale becoming so-called graphene quantum dots (GQDs), the bandgap opens up in a size-dependent manner due to the quantum confinement effect. Such emerging 0D materials are promising for a wide spectrum of applications including bio-imaging,[1-4] optical sensing,[3-7] light-emitting diodes,[8-10] photovoltaics,[10-12] photocatalysis,[13-15] energy storage[16-18] and conversion,[18, 19] *etc*. But the applications of GQDs are largely hindered by the difficulties to obtain a defined and desired bandgap suitable for a particular purpose. Most current GQDs have a bandgap between 2.2 to 3.1 eV, *i.e.*, they are usually green or blue fluorescent. Narrow-gap GQDs (yellow to red fluorescent GQDs) are not common.

Starting with wide-gap GQDs, we herein demonstrate two distinct strategies to systematically narrow the bandgap to produce a series of GQDs with varying bandgaps. Because the bandgap of pristine GQD (separation between π and π* orbitals) is inversely proportional to the size of sp2 domain,[3, 20, 21] narrowing bandgap can be achieved by conjugating GQDs with poly-aromatic rings to enlarge the π-conjugated sp2-carbon network. Alternatively, bandgap narrowing can be realized by introducing an intermediate n-orbital between π and π* orbitals *via* functionalization with electron-donating chemical groups. Many types of GQDs contain electron-withdrawing oxygenated functional groups (*e.g.*, -COOH and –CHO), conferring the GQD with p-type conductivity.[14, 22, 23] Hence upon conjugation with electron-donating chemical groups, intramolecular Z-schemes structure[24] forms on GQD, which consists of p-type oxygenated groups, n-type conjugates[14, 22, 25, 26] and sp2 Ohmic contact (mediator) in between.

Both narrow bandgap and Z-scheme structure are desirable for photocatalysis because the former ensures stronger and wider light adsorption while the latter promotes separation of photo-

excited electron-hole pairs. In this work, we demonstrate gradual bandgap narrowing of GQDs from 2.4 to 1.88 eV (green to red), and apply the narrow bandgap GQDs for photocatalytic water splitting and CO_2 reduction with high performance.

RESULTS AND DISCUSSION

As previously reported, GQDs were firstly synthesized through a one-step strong acid cutting using anthracite coal as the precursor.[27] This was followed by ultrafiltration and dialysis to obtain GQDs with an average diameter of 5.86 nm (± 1.13 nm; n = 127) and thickness of 1.19 nm (±0.31 nm, 115 samples), as shown in Figure S1 in Supporting Information (SI). The high-resolution TEM identifies the lattice spacing (0.21 nm) corresponding to graphene (100) facet.[15, 28-30] GQDs can disperse very well in water because of its extremely small size and many charged functional groups (*e.g.*, -COOH). To enlarge the π-conjugated system (essentially, the size of GQD), we conjugated GQDs with four polyaromatic compounds, specifically, o-phenylenediamine (OPD), 2,3-diaminonaphthalene (DNPT23), 1,8-diaminonaphthalene (DNPT18) and 1,1'-bi(2-naphthalene) (BNPTL), through the condensation reaction between C=O and $-NH_2$ to form C=N bond under solvothermal condition (Figure 1). Conjugated GQDs can still disperse well in water although the abundance of the charged functional groups is reduced.

In Fourier transform infrared spectroscopy (FTIR), all GQDs exhibit the bands at 3500 cm^{-1} due to O-H stretching vibration from hydroxyl groups, and at 1600 cm^{-1} due to C=C stretching from sp2 carbon network (Figure S2a in SI). Coal GQD shows a prominent C-O band at 1385 cm^{-1}, and a widened C=C band at 1600 cm^{-1} due to overlapping from C=O stretching at 1631 cm^{-1}. The four modified GQDs all display C-H band at 2900 cm^{-1} from the conjugates, 1460 cm^{-1} band due to C=N between the conjugates and GQD, and a shifted C-O band at 1380 cm^{-1}. The

large reduction of C=O vibration signal at 1631 cm^{-1} indicates the consumption of C=O sites on coal GQD by the conjugation reaction.

Full range X-ray photoelectron spectroscopy (XPS) demonstrates C 1s, O 1s and N 1s peaks at 284, 532 and 398 eV, respectively (Figure S2b in SI).[15, 31, 32] Because of its high oxygen content, original GQD can also be regarded as graphene oxide quantum dot. The (O 1s)/(C 1s) ratios are largely reduced after conjugating original GQD with OPD, DNPT23, DNPT18 and BNPTL because of C=N bond formation (Table S1 in SI). As expected, the (N 1s)/(C 1s) ratios increase from zero to ~5% after conjugating nitrogen-containing poly-aromatic compounds. Both FTIR and XPS characterizations unambiguously confirm the success of conjugation through the condensation reaction.

High-resolution C 1s spectra further confirm that the conjugation with OPD, DNPT23, DNPT18 and BNPTL apparently increases π-conjugated C=C bonds and consumes C=O bonds to generate C=N bonds (Figure S3a in SI). The N1s XPS peaks (Figure S3b) can be deconvolved into pyrazine N, pyrimidine N, amino N and amide N peaks resulting from the three reaction modes between GQD and aromatic amines (Figure S4 in SI). But note that pyrazine N is the dominating N form when a 1,4-diazine (pyrazine) ring is formed by condensation between two C=O and two ortho-amino groups (Figure 1). This observation also suggests that the other two reaction modes and physical adsorption of aromatic amines (which contributes to amino N peak) are negligible. The obtained conjugated GQDs are stable because the bonding energy of C=N is ~615 kJ/mol, decomposition of which only occur above 1200 K.

According to the increase of molecular weight after conjugation as determined by mass spectrometry (Figure S5 and S6 in SI), it is estimated that on average 4.05 OPD, 4.16 DNPT23, 4.29 DNPT18 or 3.99 BNPTL molecules are conjugated onto one GQD. This is in a good

agreement with the (N 1s)/(C 1s) ratio characterized by XPS. In a control experiment, a small aromatic molecule 1,2-benzoquinone was conjugated with OPD. As evidenced by the FTIR characterization (Figure S7 in SI), phenazine is formed as expected without apparent other by-products. This experiment proves that the used conjugation strategy works not only for GQDs (in a way they can be regarded as a giant aromatic molecule) but also small aromatic molecules.

Figure 2a presents the photographs of the aqueous dispersions of original GQD, GQD-OPD, GQD-DNPT23, GQD-DNPT18, and GQD-BNPTL under UV mercury lamp. As seen, their fluorescence varies from green to red indicating the progressive bandgap narrowing (red-shifting) while the size of the conjugated poly-aromatic ring increases. Consistently, the photoluminescence (PL) emission peaks of original GQD, GQD-OPD, GQD-DNPT23, GQD-DNPT18, and GQD-BNPTL also red-shift in order (Figure 2b). As revealed by the UV-vis absorption spectra (Figure 3a), the light adsorbing abilities are ranked as following: GQD-BNPTL > GQD-DNPT18 > GQD-DNPT23 > GQD-OPD > GQD. As compared to the original wide bandgap green GQD, the light absorption of red GQD-BNPTL, which has the narrowest bandgap among all, is much stronger and extends much further into the visible range. The strong absorption between 200–300 nm for all GQDs is due to π-π^* transition in sp^2 basal plane, which is common for all graphene materials.[33] The absorption shoulder at ~480 nm for original GQD is resulted from the electron transition from n-orbital (induced by the weak electron-donating –OH group on GQD) to π^* orbital.[2] The absorption shoulders (550 – 600 nm) for the conjugated GQDs are caused by the electron transition from n-orbital (introduced by the electron-donating pyrazine N on the conjugated moieties) to π^* orbital.[34] There is an obvious redshift of the absorption shoulder peak as the bandgap is narrowed further by conjugating GQD with a larger poly-aromatic molecule.

In the $(\alpha E)^2$ *versus* (E) plot derived from UV-vis spectrum where E is photon energy and α is the normalized adsorption coefficient, the GQD bandgap can be determined by the horizontal intercept of the extrapolation from the linear region (Figure 3b).[14, 15, 35] The bandgaps of original GQD, GQD-OPD, GQD-DNPT23, GQD-DNPT18 and GQD-BNPTL are 2.40 eV, 2.05 eV, 1.95 eV, 1.91 eV and 1.88 eV, respectively, which are consistent with their fluorescence colors. Alternatively, we utilize the linear sweep voltammetry to determine the conduction band minimum (CBM), valance band maximum (VBM), and thus bandgap (CBM - VBM) (Figure 3c-d and Table S2 in SI).[14] The bandgaps determined by both methods are in good accordance. The CBMs of GQD, GQD-OPD, GQD-DNPT23, GQD-DNPT18 and GQD-BNPTL are -1.40 eV, -1.10 eV, -1.04 eV, -1.01 eV and -0.99 eV (*vs*. Ag/AgCl) respectively, while the corresponding VBMs are 1.00 eV, 0.95 eV, 0.91 eV, 0.90 eV and 0.89 eV (*vs*. Ag/AgCl) respectively. As seen from the energy diagram in Figure 4a, conjugation of poly-aromatic rings lowers CBM (π^*) in a ring-size dependent manner while VBM remains relatively stable, whereby leading to bandgap reduction. These observations are further supported by density functional theory (DFT) calculations (Table S3 in SI).

The Mott-Schottky analysis is applied to identify the types of conductivity for each kind of GQDs.[14, 36] Linear region(s) of $1/C^2$ (C is the capacitance) *versus* the applied potential can be fitted with Mott-Schottky equation (Figure S8 and S9, Table S2 in SI). Negative linearity suggests the existence of p-type conductivity while positive linearity suggests n-type. Original GQD only manifests p-type conductivity caused by the strong electron-withdrawing oxygenated groups (*e.g.*, -COOH and -CHO) despite the co-existence of weak electron-donating –OH groups. In contrast, GQD-OPD, GQD-DNPT23, GQD-DNPT18 and GQD-BNPTL exhibit both p- and n-type of conductivity where n-type is endowed by the electron-donating pyrazine N atoms (Figure

S9 in SI). The Fermi levels of n-type conductivity (E_{Fn}) and p-type conductivity (E_{Fp}) are determined by the horizontal intercepts of the positive or negative linear extrapolations of $1/C^2$ respectively (Figure S9 and Table S2 in SI, and Figure 4a). Evidently, conjugated GQDs, but not the original GQD, possess both p-type and n-type domains. The co-existence of p- and n-type conductivities has also been previously observed in other GQDs[14, 22] and nanoparticles.[37, 38] Unlike a conventional heterojunction where p-type and n-type semiconductor are in direct physical contact or interface, the p- and n-type domains on a GQD molecule are coupled through the sp2 carbon network of the GQD basal plane, forming intramolecular Z-scheme structure.[24, 39] Such structure favors charge separation and thus coupling between photo-exited anodic and cathodic redox reactions.

Alternatively, GQD bandgap can be narrowed by introducing n-orbital between π and π* orbitals. For this, we graft GQDs with electron-donating functionalities, specifically, p-anisidine (Anln-OCH_3), 4-(trifluoromethoxy)aniline (Anln-OCF_3), and 4-(trichloromethoxy)aniline (Anln-$OCCl_3$) through the condensation reaction between -COOH and -NH_2 to form N-C=O amide bond under solvothermal condition (Figure 1). The three modified GQDs all display C-H peak (2900 cm^{-1}) from the conjugates, C=O peak (1650 cm^{-1}) and C–N peak (1456 cm^{-1}) from the formed O=C-N amide bonds between the conjugates and GQD (Figure S10a in SI).[40] The stretching vibrations of C-F[41, 42] from GQD-Anln-OCF_3 and C-Cl[43] from GQD-Anln-$OCCl_3$ are located at 1300 cm^{-1} and 750 cm^{-1}, respectively. All these observations confirm the successful functionalization.

The overall XPS spectra in Figure S10b (SI) present F 1s (686 eV)[44] for GQD-Anln-OCF_3, Cl 2p (200 eV)[45] for GQD-Anln-$OCCl_3$, and N 1s (401 eV) for all conjugated GQDs in addition to the common C 1s (284 eV) and O 1s (532 eV) peaks. The (O 1s)/(C 1s) ratio is reduced as expected after functionalization through condensation between –COOH and –NH_2. The

consequent formation of O=C–N amide bonds is evidenced by C=O and C–N peaks in high-resolution C 1s XPS spectra (Figure S11a in SI). In addition, N 1s peak at 401 eV is characteristic to amide N (Figure S11b in SI). A control experiment of conjugation between benzoic acid and aniline to form benzanilide (yield 95.2%, Figure S12 in SI) has been conducted to prove that the used conjugation strategy universally works for not only for GQDs but also for small aromatic molecules. According to the increase of molecular weight after functionalization determined by mass spectrometry (Figure S13 in SI), it is estimated that ~8.57Anln-OCH_3, ~8.60 Anln-OCF_3, and ~8.41 Anln-$OCCl_3$ are functionalized onto one GQD. This is in good agreement with the (N 1s)/(C 1s) ratios determined by XPS.

As shown in Figure 2c, the fluorescence of original GQD, GQD-Anln-OCH_3, GQD-Anln-OCF_3 and GQD-Anln-$OCCl_3$ progressively redshifts indicating gradual bandgap narrowing while the electron donating ability increases (Anln-OCH_3 < Anln-OCF_3 < Anln-$OCCl_3$) (Figure 2d). The light adsorbing abilities are ranked as GQD-Anln-$OCCl_3$ > GQD-Anln-OCF_3 > GQD-Anln-OCH_3 > GQD (Figure 5a). Specifically, compared to the original green GQD, the light adsorption of red GQD-Anln-$OCCl_3$ is much stronger and extends much further into the visible range due to bandgap narrowing. The prominent absorption peaks between 250–300 nm from GQD-Anln-OCF_3 and GQD-Anln-$OCCl_3$ (Figure 5a) could be the electron transition from n to σ* orbital (Figure 4b). The absorption shoulders (between 530-600 nm) for the functionalized GQDs are due to the electron transition from the n-orbital (induced by lone pair electrons from N, F or Cl) to π* orbital.[46] There is an apparent redshift of this absorption shoulders when the bandgap is narrowed further by the stronger electron-donating groups.

Based on the $(\alpha E)^2$ *versus* E plot (Figure 5b), the bandgaps of GQD-Anln-OCH_3, GQD-Anln-OCF_3 and GQD-Anln-$OCCl_3$ are determined as 2.08 eV, 2.02 eV, 1.94 eV, respectively, which

are narrowed from original GQD (2.40 eV). These bandgaps are in line with their fluorescence colors. Linear sweep voltammetry (Figure 5c-d) is used to identify CBM (π*) and VBM (n orbital) which are illustrated in the energy diagram shown in Figure 4b (also see Table S4 in SI).[14] The obtained bandgaps (CBM-VBM) are consistent with the values determined by Figure 5b. Mott-Schottky analysis (Figure S14 and Table S4 in SI) reveals that GQD-Anln-OCH_3, GQD-Anln-OCF_3 and GQD-Anln-$OCCl_3$ possess Z-scheme structure with both p- and n-type conductivity (their Fermi levels are indicated in Figure 4b).

The intramolecular Z-scheme structure (*i.e.*, p-type, n-type domains with sp2 Ohmic contact in between) on a functionalized GQD favors charge separation to promote coupled photocatalytic redox reactions on the same GQD molecule.[24] And because the standard redox potentials of water splitting (H^+/H_2 at -0.41 V, H_2O/O_2 at 0.82 V *vs*. NHE, pH=7)[47] and CO_2 reduction (CO_2/CH_3OH at -0.38 V *vs*. NHE, H_2O/O_2)[48, 49] are enclosed within the CBM and VBM of the GQDs, they are able to photo-catalyze these reactions (Figure 6a).

Figure 6b presents the time course (over 72 h with the system evacuated every 12 h) of H_2 evolution for each GQD type under visible light (420-800 nm). GQD-BNPTL with the narrowest bandgap (thus strongest light absorption ability and widest absorption range) gives the highest H_2 yield (130 μmol h^{-1}), which is about nine-fold higher than the original GQD. This is also higher than the previously reported graphene quantum dots,[14, 22, 50] GQD-based[51] and graphene-based composites.[52] Apparent quantum yields (AQYs) of GQD-BNPTL are 11%, 5.6%, 3.0% and 2.7% under 420, 460, 500 and 550 nm illuminations respectively. The decrease of AQYs with increasing illumination wavelength is due to decreased adsorption. As seen from Table S5 in SI, the photocatalytic performance in H_2 generation of our GQD-BNPTL offers top performance among all the carbon photocatalysts. In addition, its performance could be further improved by

hybridization with nanoparticles of noble metals, transition metal oxides / sulfides / phosphides, or metal alloys.

Figure 6c presents the time courses of CO_2 reduction to form methanol under visible light. GQD-BNPTL also offers the best performance (yield rate of 0.695 μmol h^{-1} g_{cat}^{-1}), which is about three times higher than original GQD. And the performance is superior to previously reported graphene oxide micro-sheets[53] and TiO_2 (P-25).[54] Pure carbon photocatalysts have been rarely explored for CO_2 reduction (Table S6 in SI). GQD-BNPTL as quasi-homogeneous photocatalyst offers advantages and its performance could be further improved by hybridization with other functional nanoparticles and using sacrificial reagents.

Photo-reduction reaction using isotopically labelled $^{13}CO_2$ proves that CO_2 is the only carbon source (but not GQD) for methanol production (Figure S15 in SI). The mechanism of CO_2 reduction to methanol in a 6-electron transfer process is elucidated in Figure 6a. Only a small amount of CO is generated as the byproduct (Figure S16 in SI), because the standard reduction potential for CO_2/CO (-0.53V *vs*. NHE)[55] is more negative than that of CO_2/CH_3OH. O_2 has been generated as the photo-anodic counterpart (Figure S17 in SI) for the photo-cathodic CO_2 reduction. As seen from Figure 6b and c, all GQD catalysts are rather stable against photo-corrosion.

The good performance of GQD-BNPTL is attributable to the chemical inertness of GQD, good light absorption ability, and the existence of intramolecular Z-scheme structure.[24, 56, 57] As illustrated in Figure 6d, the electrons are photo-excited from valence band (VB) to conduction band (CB) on both p-type subdomains with electron-withdrawing oxygenated groups and n-type subdomains with electron-donating nitrogen. The excited electrons on the CB of p-type subdomains are used for photo-cathodic CO_2 reduction while the holes on the VB of n-type

subdomains are consumed by photo-anodic O_2 generation. As the CB of n-type subdomains are lower than that of p-type subdomains, the photo-excited electrons there combine with the holes from the VB of p-type subdomains through the Ohmic contact (sp2 carbon network on GQD with low resistance) between the two different types of subdomains, instead of being used for CO_2 reduction. Such charge combination in the Ohmic contact promotes the photo-induced electron-hole separation in both p-type and n-type subdomains, whereby facilitates photo-cathodic reduction on p-type subdomains and photo-anodic oxidation on n-type subdomains. Similar mechanism was previously proposed by Teng *et al.* for H_2 evolution.[14] And the intra-molecular Z-scheme mechanism proposed here is consistent with the conventional Z-scheme mechanism recognized in hybridized systems.[24, 57] According to the time-resolved decay profiles (Figure S18 in SI), the lifetime of GQD-BNTPL (6.4 ns) is much longer than that of original GQD (3.1 ns) confirming that GQD-BNTPL permits much improved charge separation (*i.e.*, prevention of recombination of photo-excited electron and hole pairs) due to Z-scheme structure.

CONCLUSIONS

In summary, this study demonstrates two different strategies to systematically narrow the bandgap of GQD. Specifically, conjugating GQDs with poly-aromatic moieties to enlarge π conjugated sp2-carbon system narrows GQD bandgap (consequently increasing photoluminescence wavelength) mainly due to lowering of π* orbital. Alternatively, bandgap lowering can be achieved *via* introducing intermediate n orbital between π and π* orbitals after conjugation with electron-donating functional groups. In our functionalized GQDs, intramolecular Z-scheme structure exists, which consists of p-type and n-type domains separated by sp2-carbon Ohmic contact.

We have only selected several chemicals to demonstrate the strategies. In principle, GQD bandgap can be continuously tuned simply by changing the number and the properties of the conjugates. The former may be controlled by the reaction time or the abundance of carboxyl groups (chemical handles) on the original GQDs. Such precise bandgap engineering can make GQDs snugly suitable for particular applications. For example, a series of GQDs emitting different fluorescence wavelengths can be produced to extend the application scope of GQDs for bioimaging or fluorescence-based sensing.

Narrow bandgap of a GQD promotes light absorption fraction and range. Intramolecular Z-scheme structure assists to couple redox reactions on the same molecule by preventing the recombination of photo-excited electron-hole pairs. Taking advantages of these two features, our functionalized GQDs are utilized for water splitting and CO_2 reduction under visible light. Comparing to other photocatalysts, GQDs offer several advantages. They are synthesized from earth-abundant, cheap, and environmental friendly carbon materials. And owing to the molecular size, GQDs disperse well in aqueous solution and their active sites are fully exposed. Compared with their micro-sized counterparts (graphene oxide sheets) or bulk materials, GQDs possess a larger fraction of the active sites (mostly edges). On one hand, GQDs act as quasi-homogeneous catalysts to achieve high efficiency; on the other hand, they can be recycled for reuse.

METHODS

Synthesis of coal GQDs and Functionalization: Coal GQDs were obtained from Dotz Nano (Israel). As previously reported,[27] GQDs were prepared from anthracite coal through refluxing at 120 ^{o}C for 24 h with concentrated nitric acid and sulfuric acid, followed by cross-flow ultrafiltration (cut-off molecular weight 5 kDa). To functionalize GQDs, toluene (10 mL) containing 10 mg coal GQDs was added with o-phenylenediamine (OPD, 50 mg), 2,3-diaminonaphthalene (DNPT23, 50 mg), 1,8-diaminonaphthalene (DNPT18, 50 mg), 1,1'-bi(2-naphthylamine) (BNPTL, 50 mg), p-anisidine (Anln-OCH_3, 50 mg), 4-(trifluoromethoxy)aniline

(Anln-OCF_3, 50 mg), or 4-(trichloromethoxy)aniline (Anln-$OCCl_3$, 50 mg), followed by solvothermal reaction at 180 ^oC for 12 h in a sealed Teflon-lined autoclave. Subsequently, the resulting solutions were dialyzed with cellulose ester dialysis membrane (MWCO 500-1000 Da) to remove excessive organic molecules and toluene. Finally, the solutions were concentrated by a rotatory evaporator and freeze-dried.

Characterization: Transmission electron microscopy (TEM) and atomic force microscopy (AFM) were conducted with JEOL JEM 2010 and Bruker ICON AFM, respectively. X-ray photoelectron spectroscopy (XPS) measurement was performed on VG Multilab 2000 spectrometer (Thermo) with an Al Kα 1846.6 eV anode. C 1s peak at 284.6 eV was employed as reference to calibrate the binding energy. The Fourier-transform infrared spectroscopy (FTIR) and UV-vis absorption spectroscopy were obtained from PerkinElmer FTIR spectrometer (Spectrum One) and Shimadzu UV-2450, respectively. Photoluminescence spectroscopy and lifetime measurement were carried out by a Fluorolog TCSPC fluorescence spectrometer (HORIBA). The mass spectrometry (MS) has employed the Agilent LCMS 6130. The linear sweep voltammetry (Chenhua Electrochemical Station) was conducted at scan rate of 5 mV/s in 0.5 M Na_2SO_4 solution. The type of conductivity was determined by Mott-Schottky analysis[22] using a impedance spectrometer (Zahner IM6e, Germany) equipped with Thales software.

Density functional theory (DFT) calculation: The Gaussian 09 program package was used to conduct DFT calculation.[58] To simplify calculation without losing generality, original GQD is represented by a 7-benzene ring while functionalized GQD only contains one conjugated moiety.

Photocatalytic performance: The photocatalytic water-splitting was conducted in a gas-enclosed irradiation system equipped with an evacuation setup and 300 W Xe lamp (Newport) with a 420 nm cutoff filter. 0.1 g of GQD catalysts were dispersed in 100 mL of water containing 10 vol% TEOA, with Pt as the co-catalyst (3 wt% Pt relative to GQDs). The amounts of generated H_2 or O_2 were examined by an on-line gas chromatography (Agilent, GC Model 6890N, TCD, carrier gas argon, 0.5 nm molecular sieve column). Before irradiation, the reaction vessel was evacuated and refilled with argon for five times to fill with pure argon gas (removing air), reaching about 30 Torr, kept at 20 °C by cooling water. Monochromatic illumination at 420, 460, 500 and 550 nm were used to determine the apparent quantum yield (AQY),[15] with illumination intensity of 0.74, 1.2, 1.2 and 1.1 $mW \cdot cm^{-2}$, respectively. The irradiated area is 12.56 cm^2.

The CO_2 photo-reduction reactions were conducted in a gas-enclosed circulation system using Pyrex cell reactor. In each reaction, 0.1 g GQDs was uniformly spread on a glass reactor with the area of 4.2 cm^2. Xenon lamp (300 W) armed with a 420 nm cutoff filter (Newport) was used to irradiate the reactions. This reaction system was evacuated for several times, before purging high-purity CO_2 into the reaction system till ambient pressure. Then ultrapure water (1.0 mL) was injected into the system for humidity and electron donor. The Xe lamp was turned on after several hours when adsorption and desorption equilibrium of the gas and the photocatalyst has been attained. The gaseous products from CO_2 photo-reduction were analyzed by gas chromatography (Agilent GC 7890A, FID, carrier gas argon, Hayesep Q 80-100 column). Photo-reduction of isotopically labelled $^{13}CO_2$ was analyzed by GC-MS (Agilent, GC 6890N, MS 5973 inert).

ASSOCIATED CONTENT

The supporting information is available free of charge on the ACS Publications website at DOI: XXX.

ACKNOWLEDGEMENTS

This research was supported by AcRF tier 2 grants (MOE2014-T2-1-003 and MOE2017-T2-2-005) from Ministry of Education (Singapore).

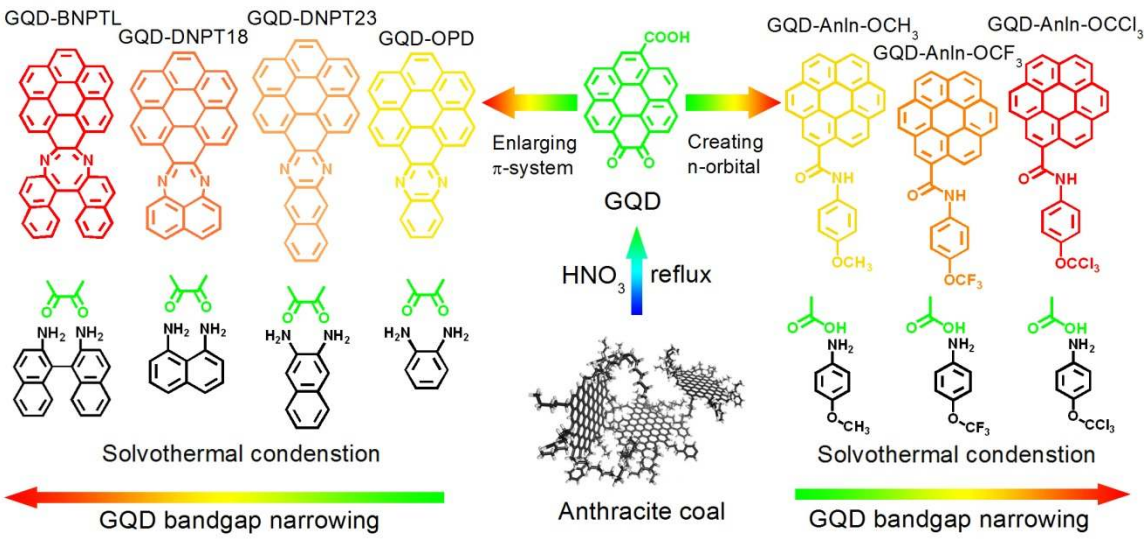

Figure 1. Illustration of bandgap narrowing by enlarging π-conjugated system *via* conjugating GQD with poly-aromatic rings or by introducing intermediate n-orbital *via* conjugating with electron-donating groups. For clarity, GQDs (contains ~60 carbon rings and various chemical groups) are over-simplified to a 7-ring structure. And for the same reason, only one conjugated moiety is illustrated for modified GQDs.

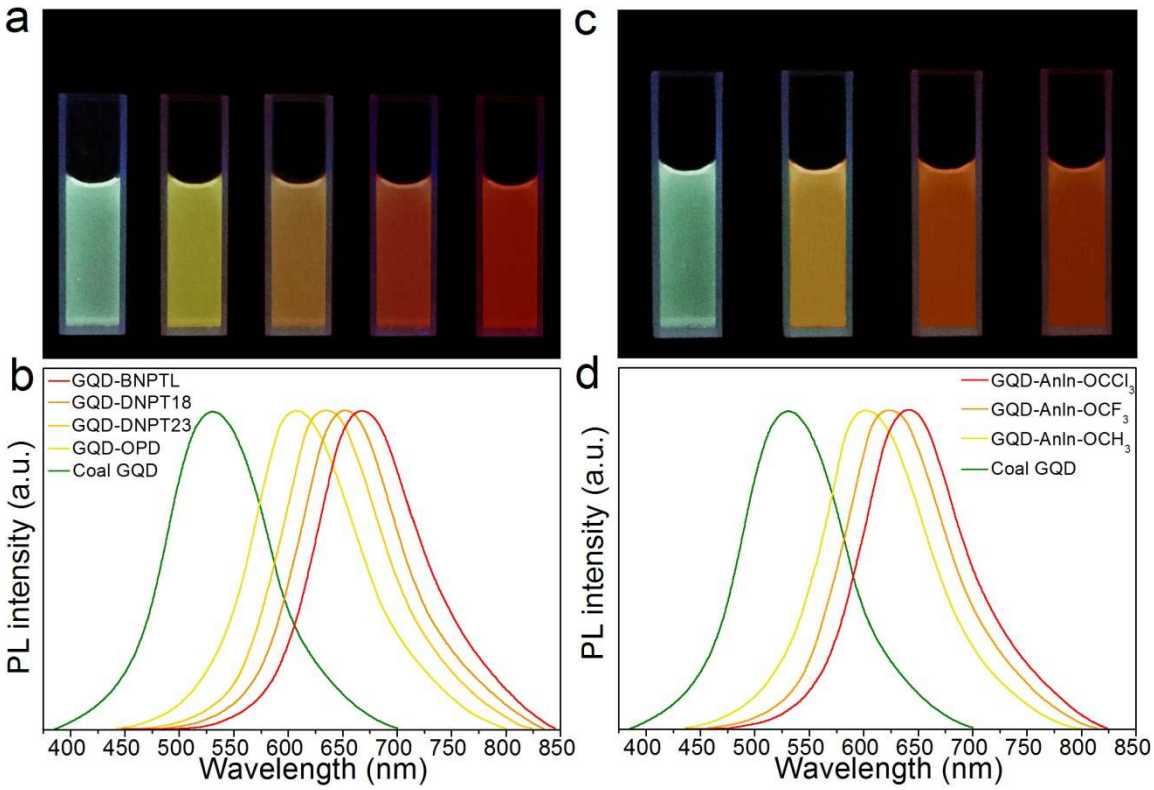

Figure 2. Photographs taken under UV mercury lamp (a) and photoluminescence spectra (b) of the aqueous solutions of coal GQD, GQD-OPD, GQD-DNPT23, GQD-DNPT18, GQD-BNPTL (from left to right, with emission peaks located at 520 nm, 610 nm, 637 nm, 652 nm, and 663 nm, respectively). And photographs taken under UV mercury lamp (c) and photoluminescence spectra (d) of the aqueous solutions of coal GQD, GQD-Anln-OCH_3, GQD-Anln-OCF_3 and GQD-Anln-$OCCl_3$ (from left to right, with emission peaks located at 598, 621 and 643 nm, respectively).

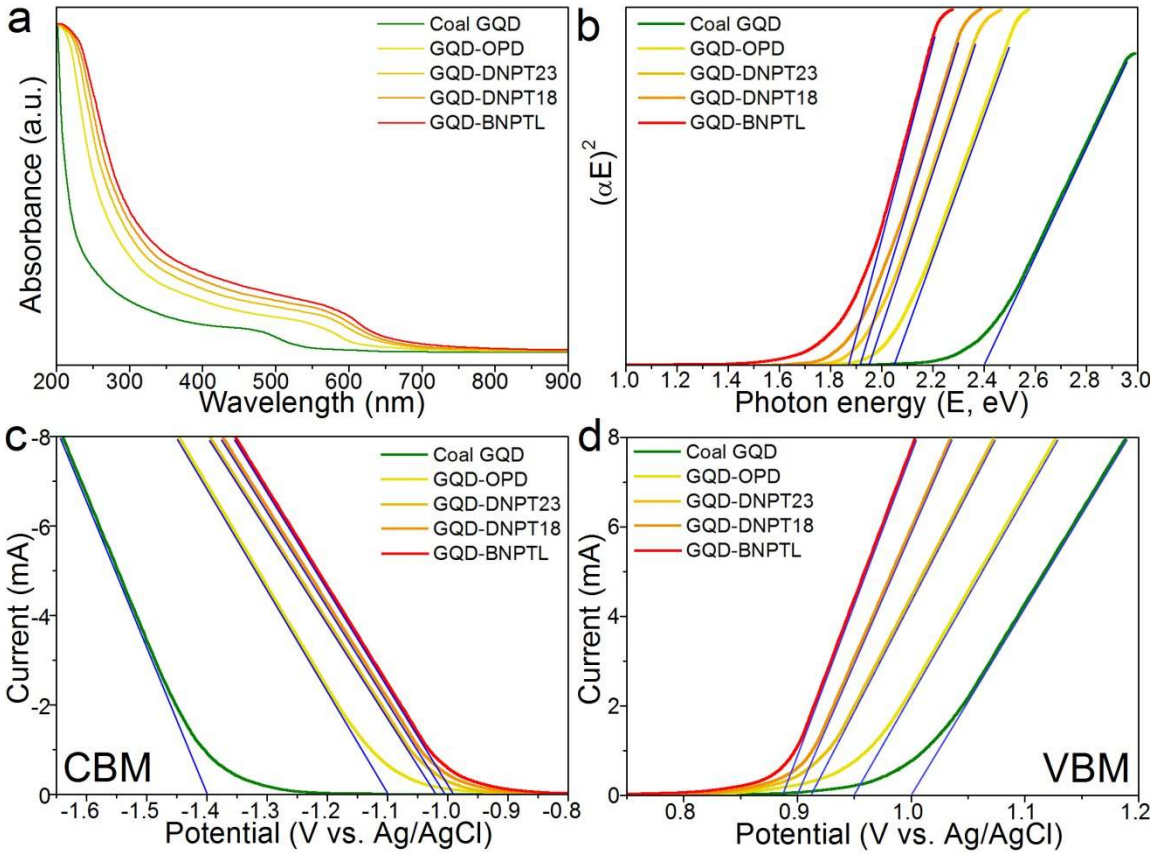

Figure 3. UV-vis absorbance spectra (a) and accordingly obtained plots (b) of $(\alpha E)^2$ *versus* photon energy (E) (where α denotes the absorbance coefficient) of coal GQD, GQD-OPD, GQD-DNPT23, GQD-DNPT18, and GQD-BNPTL. The horizontal intercept of tangent line in (b) indicates the bandgap of each GQD type. (c) Cathodic linear sweep voltammetry (c) and anodic linear sweep voltammetry (d) of coal GQD, GQD-OPD, GQD-DNPT23, GQD-DNPT18, and GQD-BNPTL. The horizontal intercept of tangent line in (c) or (d) determines the conduction band minimum (CBM) or the valence band maximum (VBM) of each GQD type, respectively.

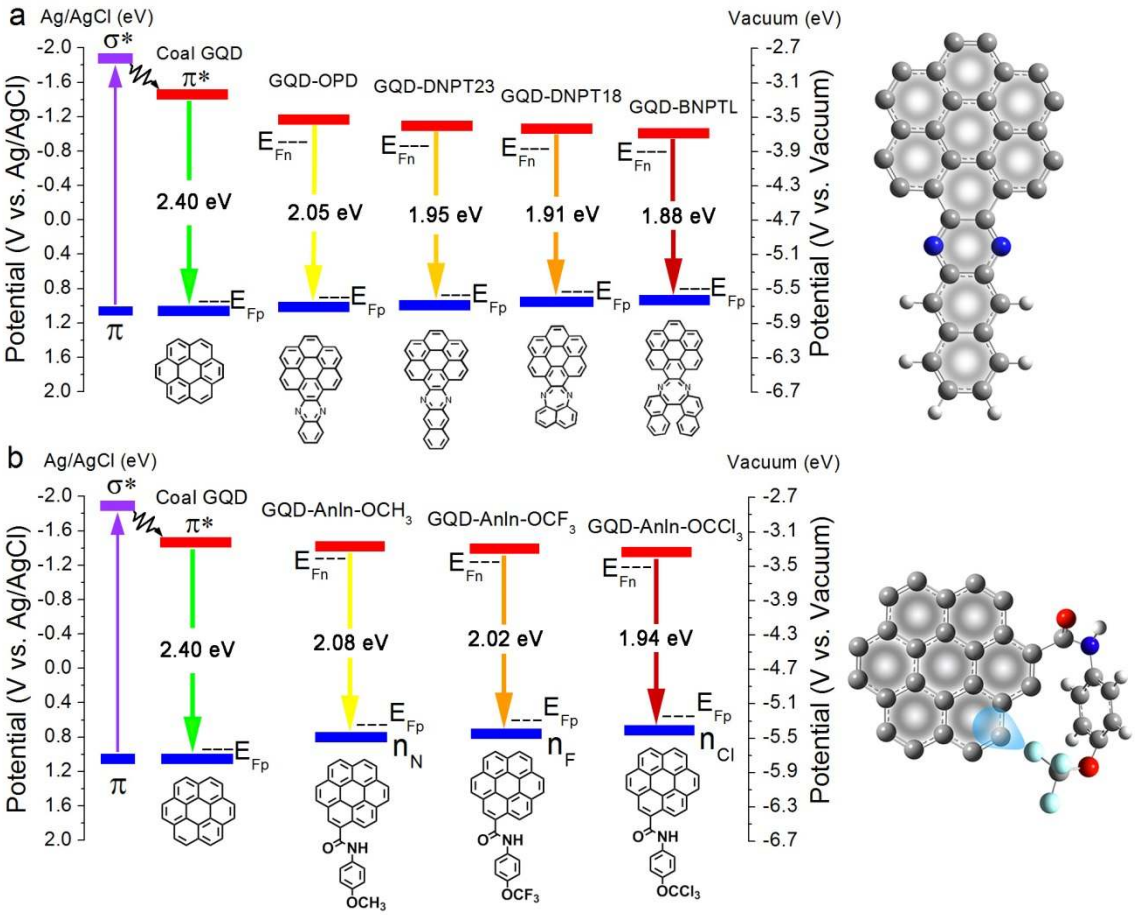

Figure 4. Illustration of energy level diagram and simplified structure of (a) coal GQD, GQD-OPD, GQD-DNPT23, GQD-DNPT18, and GQD-BNPTL, and (b) coal GQD, GQD-Anln-OCH_3, GQD-Anln-OCF_3, and GQD-Anln-$OCCl_3$. The Fermi levels for p-type conductivity (E_{Fp}) and n-type conductivity (E_{Fn}) are indicated in the energy diagram.

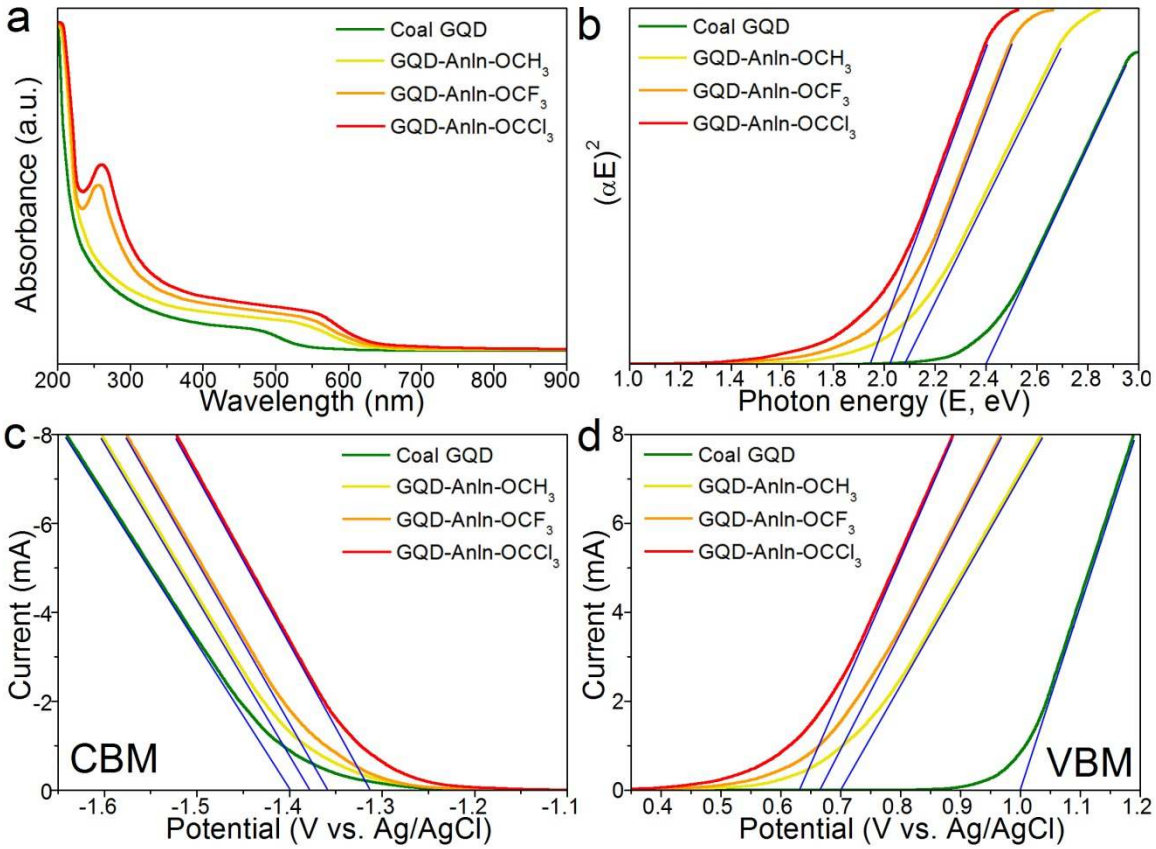

Figure 5. UV-vis absorbance spectra (a) and accordingly obtained plots (b) of $(\alpha E)^2$ *versus* photon energy (E) (where α denotes the absorbance coefficient) of coal GQD, GQD-Anln-OCH_3, GQD-Anln-OCF_3, and GQD-Anln-$OCCl_3$. The horizontal intercept of tangent line in (b) indicates the bandgap of each GQD type. (c) Cathodic linear sweep voltammetry (c) and anodic linear sweep voltammetry (d) of coal GQD, GQD-Anln-OCH_3, GQD-Anln-OCF_3, and GQD-Anln-$OCCl_3$. The horizontal intercept of tangent line in (c) or (d) determines the conduction band minimum (CBM) or the valence band maximum (VBM) of each GQD type, respectively.

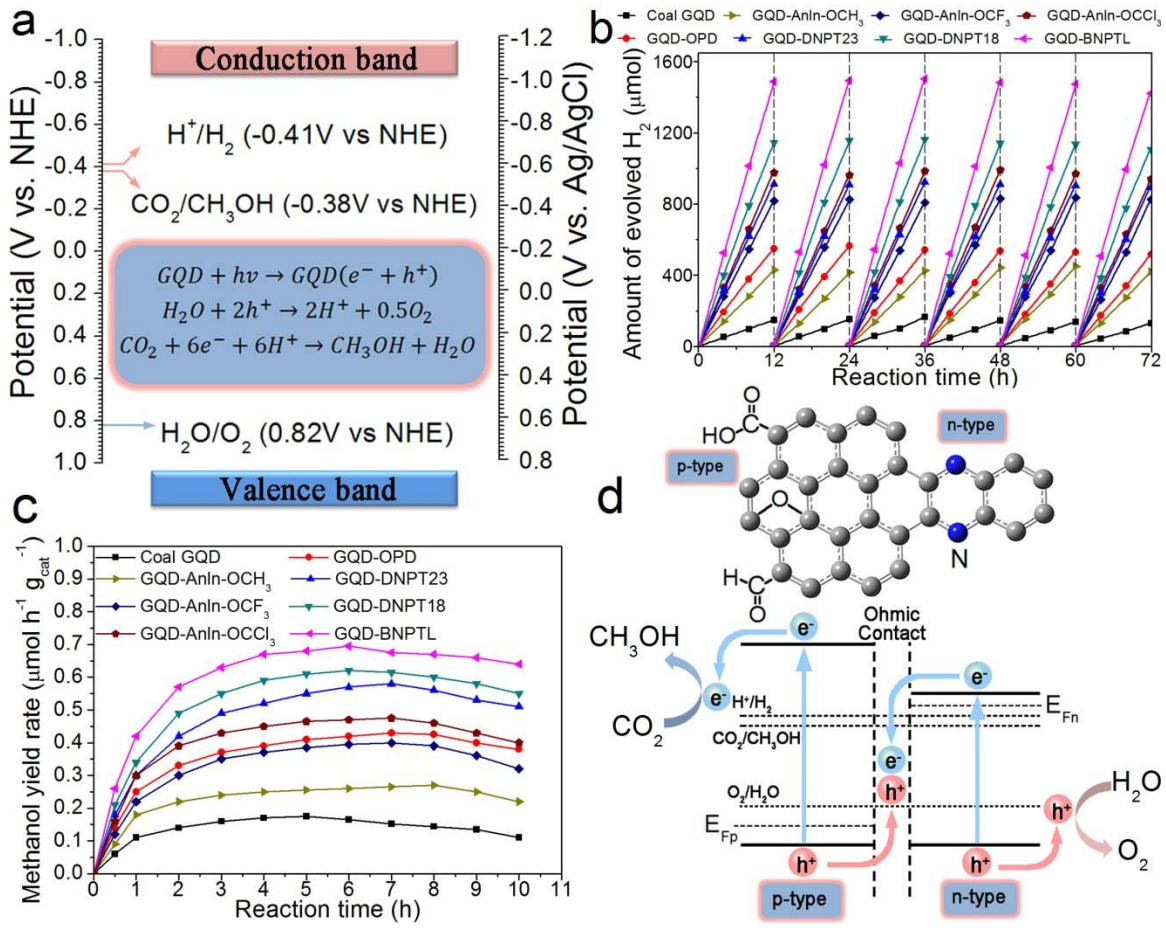

Figure 6. (a) Illustration of standard redox potentials, CBM and VBM of GQD, and CO_2 reduction process. (b and c) Time courses of H_2 evolution (b) and CO_2 reduction (c) of all GQD types under visible light (420-800 nm). (d) Schematic illustration of GQD Z-scheme based photocatalysis of CO_2 reduction.

REFERENCES

(1) Ge, J. C.; Lan, M. H.; Zhou, B. J.; Liu, W. M.; Guo, L.; Wang, H.; Jia, Q. Y.; Niu, G. L.; Huang, X.; Zhou, H. Y.; Meng, X. M.; Wang, P. F.; Lee, C. S.; Zhang, W. J.; Han, X. D., A Graphene Quantum Dot Photodynamic Therapy Agent with High Singlet Oxygen Generation. *Nat. Commun.* **2014,** *5*, 4596.

(2) Chen, J.; Than, A.; Li, N.; Ananthanarayanan, A.; Zheng, X.; Xi, F.; Liu, J.; Tian, J.; Chen, P., Sweet Graphene Quantum Dots for Imaging Carbohydrate Receptors in Live Cells. *FlatChem* **2017,** *5*, 25-32.

(3) Zheng, X. T.; Ananthanarayanan, A.; Luo, K. Q.; Chen, P., Glowing Graphene Quantum Dots and Carbon Dots: Properties, Syntheses, and Biological Applications. *Small* **2015,** *11*, 1620-1636.

(4) Li, L. L.; Ji, J.; Fei, R.; Wang, C. Z.; Lu, Q.; Zhang, J. R.; Jiang, L. P.; Zhu, J. J., A Facile Microwave Avenue to Electrochemiluminescent Two-Color Graphene Quantum Dots. *Adv. Funct. Mater.* **2012,** *22*, 2971-2979.

(5) Ananthanarayanan, A.; Wang, X. W.; Routh, P.; Sana, B.; Lim, S.; Kim, D. H.; Lim, K. H.; Li, J.; Chen, P., Facile Synthesis of Graphene Quantum Dots from 3D Graphene and their Application for Fe^{3+} Sensing. *Adv. Funct. Mater.* **2014,** *24*, 3021-3026.

(6) Li, N.; Than, A.; Sun, C. C.; Tian, J. Q.; Chen, J.; Pu, K. Y.; Dong, X. C.; Chen, P., Monitoring Dynamic Cellular Redox Homeostasis Using Fluorescence-Switchable Graphene Quantum Dots. *Acs Nano* **2016,** *10*, 11475-11482.

(7) Li, N.; Than, A.; Wang, X. W.; Xu, S. H.; Sun, L.; Duan, H. W.; Xu, C. J.; Chen, P., Ultrasensitive Profiling of Metabolites Using Tyramine-Functionalized Graphene Quantum Dots. *Acs Nano* **2016,** *10*, 3622-3629.

(8) Luo, Z. M.; Qi, G. Q.; Chen, K. Y.; Zou, M.; Yuwen, L. H.; Zhang, X. W.; Huang, W.; Wang, L. H., Microwave-Assisted Preparation of White Fluorescent Graphene Quantum Dots as a Novel Phosphor for Enhanced White-Light-Emitting Diodes. *Adv. Funct. Mater.* **2016,** *26*, 2739-2744.

(9) Son, D. I.; Kwon, B. W.; Park, D. H.; Seo, W. S.; Yi, Y.; Angadi, B.; Lee, C. L.; Choi, W. K., Emissive ZnO-Graphene Quantum Dots for White-Light-Emitting Diodes. *Nat. Nanotechnol.* **2012,** *7*, 465-471.

(10) Li, X. M.; Rui, M. C.; Song, J. Z.; Shen, Z. H.; Zeng, H. B., Carbon and Graphene Quantum Dots for Optoelectronic and Energy Devices: A Review. *Adv. Funct. Mater.* **2015,** *25*, 4929-4947.

(11) Li, Y.; Hu, Y.; Zhao, Y.; Shi, G. Q.; Deng, L. E.; Hou, Y. B.; Qu, L. T., An Electrochemical Avenue to Green-Luminescent Graphene Quantum Dots as Potential Electron-Acceptors for Photovoltaics. *Adv. Mater.* **2011,** *23*, 776-780.

(12) Tetsuka, H.; Nagoya, A.; Fukusumi, T.; Matsui, T., Molecularly Designed, Nitrogen-Functionalized Graphene Quantum Dots for Optoelectronic Devices. *Adv. Mater.* **2016,** *28*, 4632-4638.

(13) Zhuo, S.; Shao, M.; Lee, S.-T., Upconversion and Downconversion Fluorescent Graphene Quantum Dots: Ultrasonic Preparation and Photocatalysis. *Acs Nano* **2012,** *6*, 1059-1064.

(14) Yeh, T. F.; Teng, C. Y.; Chen, S. J.; Teng, H. S., Nitrogen-Doped Graphene Oxide Quantum Dots as Photocatalysts for Overall Water-Splitting under Visible Light Illumination. *Adv. Mater.* **2014,** *26*, 3297-3303.

(15) Chen, L. C.; Teng, C. Y.; Lin, C. Y.; Chang, H. Y.; Chen, S. J.; Teng, H. S., Architecting Nitrogen Functionalities on Graphene Oxide Photocatalysts for Boosting Hydrogen Production in Water Decomposition Process. *Adv. Energy Mater.* **2016,** *6*, 1600719.
(16) Lee, K.; Lee, H.; Shin, Y.; Yoon, Y.; Kim, D., Highly Transparent and Flexible Supercapacitors Using Graphene-Graphene Quantum Dots Chelate. *Nano Energy* **2016,** *26*, 746-754.
(17) Liu, W. W.; Feng, Y. Q.; Yan, X. B.; Chen, J. T.; Xue, Q. J., Superior Micro-Supercapacitors Based on Graphene Quantum Dots. *Adv. Funct. Mater.* **2013,** *23*, 4111-4122.
(18) Wang, X. W.; Sun, G. Z.; Li, N.; Chen, P., Quantum Dots Derived from Two-Dimensional Materials and Their Applications for Catalysis and Energy. *Chem. Soc. Rev.* **2016,** *45*, 2239-2262.
(19) Zhang, Z. P.; Zhang, J.; Chen, N.; Qu, L. T., Graphene Quantum Dots: An Emerging Material for Energy-Related Applications and Beyond. *Energy Environ. Sci.* **2012,** *5*, 8869-8890.
(20) Sk, M. A.; Ananthanarayanan, A.; Huang, L.; Lim, K. H.; Chen, P., Revealing the Tunable Photoluminescence Properties of Graphene Quantum Dots. *J. Mater. Chem. C* **2014,** *2*, 6954-6960.
(21) Eda, G.; Lin, Y. Y.; Mattevi, C.; Yamaguchi, H.; Chen, H. A.; Chen, I. S.; Chen, C. W.; Chhowalla, M., Blue Photoluminescence from Chemically Derived Graphene Oxide. *Adv. Mater.* **2010,** *22*, 505-509.
(22) Yeh, T. F.; Chen, S. J.; Teng, H. S., Synergistic Effect of Oxygen and Nitrogen Functionalities for Graphene-Based Quantum Dots Used in Photocatalytic H_2 Production from Water Decomposition. *Nano Energy* **2015,** *12*, 476-485.
(23) Yu, X.; Cheng, H.; Zhang, M.; Zhao, Y.; Qu, L.; Shi, G., Graphene-Based Smart Materials. *Nat. Rev. Mater.* **2017,** *2*, 17046.
(24) Zhou, P.; Yu, J. G.; Jaroniec, M., All-Solid-State Z-Scheme Photocatalytic Systems. *Adv. Mater.* **2014,** *26*, 4920-4935.
(25) Chang, D. W.; Lee, E. K.; Park, E. Y.; Yu, H.; Choi, H.-J.; Jeon, I.-Y.; Sohn, G.-J.; Shin, D.; Park, N.; Oh, J. H.; Dai, L.; Baek, J.-B., Nitrogen-Doped Graphene Nanoplatelets from Simple Solution Edge-Functionalization for n-Type Field-Effect Transistors. *J. Am. Chem. Soc.* **2013,** *135*, 8981-8988.
(26) Jin, Z.; Yao, J.; Kittrell, C.; Tour, J. M., Large-Scale Growth and Characterizations of Nitrogen-Doped Monolayer Graphene Sheets. *Acs Nano* **2011,** *5*, 4112-4117.
(27) Ye, R. Q.; Xiang, C. S.; Lin, J.; Peng, Z. W.; Huang, K. W.; Yan, Z.; Cook, N. P.; Samuel, E. L. G.; Hwang, C. C.; Ruan, G. D.; Ceriotti, G.; Raji, A. R. O.; Marti, A. A.; Tour, J. M., Coal as An Abundant Source of Graphene Quantum Dots. *Nat. Commun.* **2013,** *4*, 2943.
(28) Stankovich, S.; Dikin, D. A.; Dommett, G. H. B.; Kohlhaas, K. M.; Zimney, E. J.; Stach, E. A.; Piner, R. D.; Nguyen, S. T.; Ruoff, R. S., Graphene-Based Composite Materials. *Nature* **2006,** *442*, 282-286.
(29) Park, S.; An, J. H.; Piner, R. D.; Jung, I.; Yang, D. X.; Velamakanni, A.; Nguyen, S. T.; Ruoff, R. S., Aqueous Suspension and Characterization of Chemically Modified Graphene Sheets. *Chem. Mater.* **2008,** *20*, 6592-6594.
(30) Elias, D. C.; Nair, R. R.; Mohiuddin, T. M. G.; Morozov, S. V.; Blake, P.; Halsall, M. P.; Ferrari, A. C.; Boukhvalov, D. W.; Katsnelson, M. I.; Geim, A. K.; Novoselov, K. S., Control of Graphene's Properties by Reversible Hydrogenation: Evidence for Graphane. *Science* **2009,** *323*, 610-613.

(31) Stankovich, S.; Dikin, D. A.; Piner, R. D.; Kohlhaas, K. A.; Kleinhammes, A.; Jia, Y.; Wu, Y.; Nguyen, S. T.; Ruoff, R. S., Synthesis of Graphene-Based Nanosheets *via* Chemical Reduction of Exfoliated Graphite Oxide. *Carbon* **2007,** *45*, 1558-1565.
(32) He, H. K.; Gao, C., General Approach to Individually Dispersed, Highly Soluble, and Conductive Graphene Nanosheets Functionalized by Nitrene Chemistry. *Chem. Mater.* **2010,** *22*, 5054-5064.
(33) Pan, D. Y.; Zhang, J. C.; Li, Z.; Wu, M. H., Hydrothermal Route for Cutting Graphene Sheets into Blue-Luminescent Graphene Quantum Dots. *Adv. Mater.* **2010,** *22*, 734-738.
(34) Kwon, W.; Kim, Y. H.; Kim, J. H.; Lee, T.; Do, S.; Park, Y.; Jeong, M. S.; Lee, T. W.; Rhee, S. W., High Color-Purity Green, Orange, and Red Light-Emitting Didoes Based on Chemically Functionalized Graphene Quantum Dots. *Sci. Rep.* **2016,** *6*, 24205.
(35) Lee, K.-T.; Chuah, X.-F.; Cheng, Y.-C.; Lu, S.-Y., Pt Coupled $ZnFe_2O_4$ Nanocrystals as A Breakthrough Photocatalyst for Fenton-Like Processes - Photodegradation Treatments from Hours to Seconds. *J. Mater. Chem. A* **2015,** *3*, 18578-18585.
(36) Nian, J. N.; Tsai, C. C.; Lin, P. C.; Teng, H. S., Elucidating the Conductivity-Type Transition Mechanism of p-Type Cu_2O Films from Electrodeposition. *Journal of the Electrochemical Society* **2009,** *156*, H567-H573.
(37) Martha, S.; Mansingh, S.; Parida, K. M.; Thirumurugan, A., Exfoliated Metal Free Homojunction Photocatalyst Prepared by A Biomediated Route for Enhanced Hydrogen Evolution and Rhodamine B Degradation. *Materials Chemistry Frontiers* **2017,** *1*, 1641-1653.
(38) Etogo, A.; Liu, R.; Ren, J.; Qi, L.; Zheng, C.; Ning, J.; Zhong, Y.; Hu, Y., Facile One-Pot Solvothermal Preparation of Mo-Doped Bi_2WO_6 Biscuit-Like Microstructures for Visible-Light-Driven Photocatalytic Water Oxidation. *J. Mater. Chem. A* **2016,** *4*, 13242-13250.
(39) Low, J.; Jiang, C.; Cheng, B.; Wageh, S.; Al-Ghamdi, A. A.; Yu, J., A Review of Direct Z-Scheme Photocatalysts. *Small Methods* **2017,** *1*, 1700080.
(40) Ryu, J.; Lee, E.; Lee, S.; Jang, J., Fabrication of Graphene Quantum Dot-Decorated Graphene Sheets *via* Chemical Surface Modification. *Chem. Commun.* **2014,** *50*, 15616-15618.
(41) Brassard, J. D.; Sarkar, D. K.; Perron, J., Synthesis of Monodisperse Fluorinated Silica Nanoparticles and Their Superhydrophobic Thin Films. *Acs Appl. Mater. Interfaces* **2011,** *3* (9), 3583-3588.
(42) Wang, J. K.; Xiong, G. M.; Zhu, M. M.; Ozyilmaz, B.; Neto, A. H. C.; Tan, N. S.; Choong, C., Polymer-Enriched 3D Graphene Foams for Biomedical Applications. *Acs Appl. Mater. Interfaces* **2015,** *7*, 8275-8283.
(43) Voyiatzis, G. A.; Andrikopoulos, K. S.; Papatheodorou, G. N.; Kamitsos, E. I.; Chryssikos, G. D.; Kapoutsis, J. A.; Anastasiadis, S. H.; Fytas, G., Polarized Resonance Raman and FTIR Reflectance Spectroscopic Investigation of The Molecular Orientation in Industrial Poly(vinyl chloride) Specimens. *Macromolecules* **2000,** *33*, 5613-5623.
(44) Wheeler, V.; Garces, N.; Nyakiti, L.; Myers-Ward, R.; Jernigan, G.; Culbertson, J.; Eddy, C.; Gaskill, D. K., Fluorine Functionalization of Epitaxial Graphene for Uniform Deposition of Thin High-Kappa Dielectrics. *Carbon* **2012,** *50*, 2307-2314.
(45) Aldissi, M.; Armes, S. P., X-Ray Photoelectron-Spectroscopy Study of Bulk and Colloidal Polyaniline. *Macromolecules* **1992,** *25*, 2963-2968.
(46) Yeh, T. F.; Huang, W. L.; Chung, C. J.; Chiang, I. T.; Chen, L. C.; Chang, H. Y.; Su, W. C.; Cheng, C.; Chen, S. J.; Teng, H. S., Elucidating Quantum Confinement in Graphene Oxide Dots Based On Excitation-Wavelength-Independent Photoluminescence. *J. Phys. Chem. Lett.* **2016,** *7*, 2087-2092.

(47) Tahir, M.; Amin, N. S., Advances in Visible Light Responsive Titanium Oxide-Based Photocatalysts for CO_2 Conversion to Hydrocarbon Fuels. *Energy Convers. Manage.* **2013,** *76*, 194-214.
(48) Tu, W. G.; Zhou, Y.; Zou, Z. G., Photocatalytic Conversion of CO_2 into Renewable Hydrocarbon Fuels: State-of-The-Art Accomplishment, Challenges, and Prospects. *Adv. Mater.* **2014,** *26*, 4607-4626.
(49) Li, X.; Yu, J. G.; Wageh, S.; Al-Ghamdi, A. A.; Xie, J., Graphene in Photocatalysis: A Review. *Small* **2016,** *12*, 6640-6696.
(50) Qu, D.; Sun, Z. C.; Zheng, M.; Li, J.; Zhang, Y. Q.; Zhang, G. Q.; Zhao, H. F.; Liu, X. Y.; Xie, Z. G., Three Colors Emission from S,N Co-Doped Graphene Quantum Dots for Visible Light H_2 Production and Bioimaging. *Adv. Opt. Mater.* **2015,** *3*, 360-367.
(51) Zou, J.-P.; Wang, L.-C.; Luo, J.; Nie, Y.-C.; Xing, Q.-J.; Luo, X.-B.; Du, H.-M.; Luo, S.-L.; Suib, S. L., Synthesis and Efficient Visible Light Photocatalytic H_2 Evolution of A Metal-Free g-C_3N_4/Graphene Quantum Dots Hybrid Photocatalyst. *Appl. Catal. B-Environ.* **2016,** *193*, 103-109.
(52) Tu, W. G.; Zhou, Y.; Zou, Z. G., Versatile Graphene-Promoting Photocatalytic Performance of Semiconductors: Basic Principles, Synthesis, Solar Energy Conversion, and Environmental Applications. *Adv. Funct. Mater.* **2013,** *23*, 4996-5008.
(53) Hsu, H. C.; Shown, I.; Wei, H. Y.; Chang, Y. C.; Du, H. Y.; Lin, Y. G.; Tseng, C. A.; Wang, C. H.; Chen, L. C.; Lin, Y. C.; Chen, K. H., Graphene Oxide as A Promising Photocatalyst for CO_2 to Methanol Conversion. *Nanoscale* **2013,** *5*, 262-268.
(54) Shown, I.; Hsu, H. C.; Chang, Y. C.; Lin, C. H.; Roy, P. K.; Ganguly, A.; Wang, C. H.; Chang, J. K.; Wu, C. I.; Chen, L. C.; Chen, K. H., Highly Efficient Visible Light Photocatalytic Reduction of CO_2 to Hydrocarbon Fuels by Cu-Nanoparticle Decorated Graphene Oxide. *Nano Lett.* **2014,** *14*, 6097-6103.
(55) Habisreutinger, S. N.; Schmidt-Mende, L.; Stolarczyk, J. K., Photocatalytic Reduction of CO_2 on TiO_2 and Other Semiconductors. *Angew. Chem. Int. Edit.* **2013,** *52*, 7372-7408.
(56) Tachibana, Y.; Vayssieres, L.; Durrant, J. R., Artificial Photosynthesis for Solar Water-Splitting. *Nat. Photonics* **2012,** *6*, 511-518.
(57) Maeda, K., Z-Scheme Water Splitting Using Two Different Semiconductor Photocatalysts. *Acs Catal.* **2013,** *3*, 1486-1503.
(58) Frisch, M.; Trucks, G.; Schlegel, H. B.; Scuseria, G.; Robb, M.; Cheeseman, J.; Scalmani, G.; Barone, V.; Mennucci, B.; Petersson, G., Gaussian 09, revision a. 02, gaussian. *Inc., Wallingford, CT* **2009,** *200*.

Table of Contents Graphic

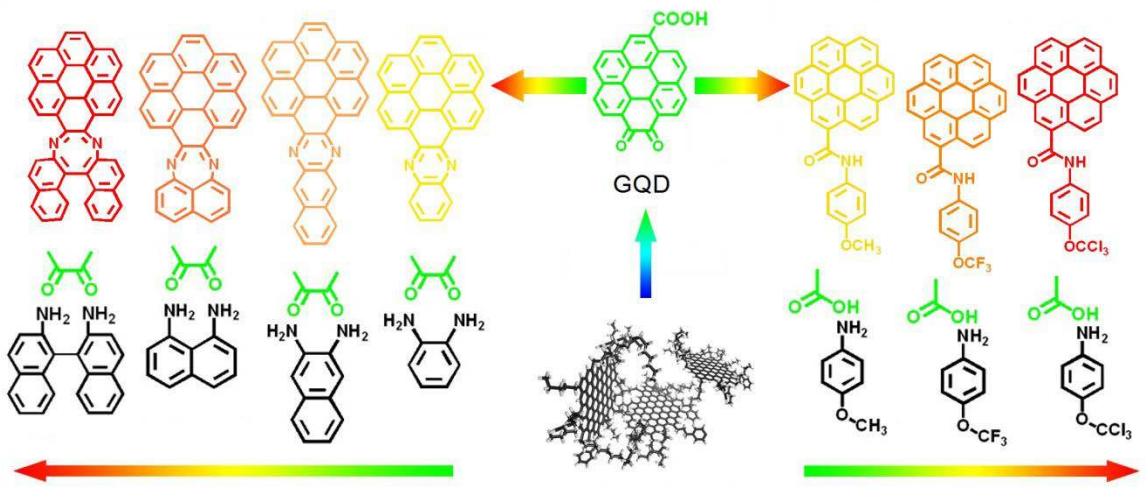

Two distinct strategies are developed to systematically narrow the bandgap of graphene quantum dots (GQDs). GQDs with narrowed bandgap and intramolecular Z-scheme structure have been employed for photocatalytic water splitting and CO_2 reduction.